ADVANCED FUNCTIONAL MATERIALS
www.afm-journal.de

Interface and Surface Cation Stoichiometry Modified by Oxygen Vacancies in Epitaxial Manganite Films

Zhipeng Li, Michel Bosman, Zhen Yang, Peng Ren, Lan Wang, Liang Cao, Xiaojiang Yu, Chang Ke, Mark B. H. Breese, Andrivo Rusydi, Weiguang Zhu,* Zhili Dong,* and Yong Lim Foo**

Perovskite manganites are viewed as one of the key building blocks of oxide spintronics devices due to their attractive physical properties. However, cation off-stoichiometry at epitaxial interfaces between manganites and other materials can lead to interfacial dead layers, severely reducing the device performance. Here, transmission electron microscopy and synchrotron-based spectroscopy are used to demonstrate that oxygen vacancies during growth serve as a critical factor for modifying the cation stoichiometry in pulsed laser deposited $La_{0.8}Sr_{0.2}MnO_3$ films. Near the film/substrate ($SrTiO_3$) interface, A-site cations (La/Sr) are in excess when oxygen vacancies are induced during film growth, partially substituting Mn. Simultaneously, Sr cations migrate towards the film surface and form a SrO rock-salt monolayer. Consequentially, a gradient of the Mn nominal valence is observed along the film growth direction, leading to anomalous magnetic properties. The results narrow the selection range of useful oxygen pressures during deposition and demonstrate that accurate cation stoichiometry can only be achieved after oxygen vacancies are eliminated during growth. This finding suggests that the oxygen pressure serves as a tuning parameter for the interfacial dead layers and, hence, for control over device properties.

Z. P. Li, Prof. Z. L. Dong
School of Materials Science and Engineering
Nanyang Technological University
Singapore 639798, Singapore
E-mail: zldong@ntu.edu.sg
M. Bosman, Prof. Y. L. Foo
Institute of Materials Research and Engineering
Agency for Science, Technology and Research (A*STAR)
3 Research Link, Singapore 117602, Singapore
Email: michel.bosman@gmail.com; yl-foo@imre.a-star.edu.sg
Z. Yang, C. Ke, Prof. W. G. Zhu
School of Electrical and Electronic Engineering
Nanyang Technological University
Singapore 639798, Singapore
Email: ewzhu@ntu.edu.sg
P. Ren, Prof. L. Wang
Division of Physics and Applied Physics
School of Physical and Mathematical Sciences
Nanyang Technological University
Singapore 637371, Singapore
L. Cao, X. J. Yu, Prof. M. B. H. Breese, Prof. A. Rusydi
Physics Department
Faculty of Science
National University of Singapore
2 Science Drive 3, 117551, Singapore

DOI: 10.1002/adfm.201200143

1. Introduction

Strontium-doped lanthanum manganites ($La_{1-x}Sr_xMnO_3$) exhibit desirable tunable properties such as colossal magnetoresistance (CMR) and half metallicity, that provide rich opportunities for multifunctional devices.[1] With a Curie temperature of 370 K, they are one of the most promising candidate materials to serve as electrodes in multiferroic tunnel junctions by combining their tunneling magnetoresistance (TMR) with electroresistance (ER) effects,[2,3] as spin injectors in polymers,[4] and in solid oxide fuel cells,[5] due to their chemical stability and near-lattice match with other functional oxides. However, the TMR of manganites decreases rapidly with increasing temperatures to low values at room temperature. One possible reason for this unwanted effect is the suppressed ferromagnetic ordering near the interface due to interface reconstruction, resulting in an electrical dead layer.[6,7] Since the physical properties of manganites strongly depend on their local chemical composition,[8] extrinsic effects such as the cation off-stoichiometry and the resulting interfacial crystalline imperfections could also lead to insulating and nonmagnetic layers. Thin manganite films with well-controlled chemical stoichiometry down to nanometer length scales are therefore required to improve performance of oxide spintronics devices.

Similar to other perovskite materials,[9–11] the stoichiometry of manganite films can be varied greatly, depending on the thin film growth conditions. Although oxygen nonstoichiometry can be removed by post-deposition annealing, cation mobility is very limited in close packed perovskite structures, which restricts their recovery to stoichiometric composition.[12] Hence, the precise control of film growth conditions and the analysis of the corresponding cation stoichiometry in films ought to receive close attention so as to achieve the desired properties. As revealed by Muller et al.[13] and Kourkoutis et al.[14] using advanced atomic-resolution electron energy-loss spectroscopy (EELS),[15] the laser fluence on ceramic targets will be decisive for the local stoichiometry of pulsed laser deposition (PLD) -grown (La,Sr)MnO_3/$SrTiO_3$ multilayers. The quality of multilayers will deteriorate with increasing laser fluence, resulting in non-stoichiometric

A-site (La and Sr) and B-site (Mn) cations, which leads to the suppression of interface magnetism. The question then arises, how can the cation stoichiometry be modified, if we tune another main film growth parameter, oxygen pressure? In the vast available literature, the accepted selection of oxygen pressure during manganite film growth can be divided into two groups: films grown with oxygen pressure above 26 Pa, with or without post-annealing,[16] and films grown with oxygen pressure around 1 Pa, resulting in films with oxygen vacancies, followed by post-annealing to recover the oxygen stoichiometry.[17] It is worth considering that the tendency to neutralize the positive charges brought by oxygen vacancies during film growth may serve as a driving force for local cation nonstoichiometry which is difficult to recover by annealing. Fister et al. observed that the strontium surface segregation in $La_{0.7}Sr_{0.3}MnO_3$ thin films increases as oxygen partial pressure decreases, implying that oxygen vacancies are somehow involved in the cation nonstoichiometry.[18] In this study, detailed investigation is carried out to form a complete picture of the effects of oxygen vacancies during film growth, on the local cation stoichiometry, the variation of the Mn valence in the epitaixal films, and their impact on the electrical and magnetic properties.

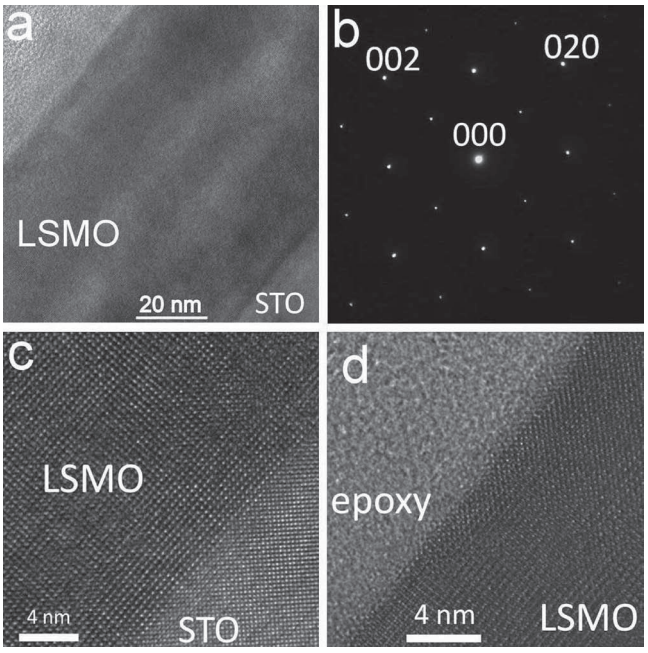

Figure 1. Morphology of the annealed LSMO thin film. a) An overview at low magnification. b) Selected-area electron diffraction pattern of the LSMO film at the [100] zone axis. c) HRTEM image of the interface of LSMO with the $SrTiO_3$ substrate. d) HRTEM image of the LSMO surface.

2. Results and Discussion

2.1. Microstructure Analysis

Details on the growth conditions of the studied films are specified in the Experimental section. The two-dimensional layer-by-layer growth mode was monitored by intensity oscillations of the reflected high energy electron diffraction (RHEED) during pulsed laser deposition of $La_{0.8}Sr_{0.2}MnO_3$ (LSMO) film, as described earlier.[19] High-resolution X-ray diffraction (HRXRD) reciprocal space mapping (RSM) directly measures the in-plane and out-of-plane lattice parameters, strain, as well as the mosaicity of the grown film. The reciprocal space mapping around the (103) plane of the as-grown film indicates its fully strained state. Additionally, an exceptionally low full-width at half maximum of 0.02° was measured by the thin film rocking curve, showing that the film is of high quality and low mosaicity. Based on the HRXRD measurements, the in-plane and out-of-plane spacing of the thin film are a = 0.3905 nm and c = 0.393 nm respectively.

Here, we present transmission electron microscopy (TEM) studies of the annealed thin film, demonstrating its monocrystallinity with high epitaxial quality and excluding the presence of grains/domains that can contribute to degradation in electrical and magnetic properties. **Figure 1**a shows a low magnification cross-sectional TEM image of the LSMO/STO couple. The micrograph was imaged with the specimen tilted to the [100] zone axis of STO. From the TEM images, there is no evidence for the formation of lamellae structures or domains, such as those discussed by Lebedev et al.[20] and Zhang et al.[21]. This point is further confirmed by the SAED pattern in Figure 1b, taken from the LSMO film. The diffraction spots of LSMO are sharp spots rather than curved, implying that the pseudocubic structures are not domain-oriented. High resolution TEM in Figure 1c reveals that the interface between LSMO and STO substrate is atomically sharp, and nearly free of misfit dislocations, in agreement with RSM. Figure 1d shows that the high epitaxial quality is maintained throughout the film until the surface; no grain boundaries were found.

2.2. EELS Analysis of the Local Mn Valence and Chemical Composition

According to the phase diagram of $La_{1-x}Sr_xMnO_3$, its electrical and magnetic properties are strongly dependent on the Mn nominal valence, which is strongly correlated with the stoichiometry of each element.[1] Therefore, to study the effect of oxygen vacancies during film growth on the local cation stoichiometry, EELS line scans were used to characterize not only the cations content profiles but also the local Mn valence along the thickness of two LSMO films. Firstly, there is a reference sample, grown under high oxygen pressure (26 Pa). After high temperature oxygen annealing, there is no change in its electrical and magnetic properties, thus we can conclude that most of the oxygen vacancies were eliminated during growth. This sample shows bulk single crystal properties, and it is believed to have nearly ideal stoichiometry.[22] The second sample is a LSMO film grown under low oxygen pressure (1 Pa). The as-grown film and the one after oxygen annealing show completely different physical properties, suggesting the formation of oxygen vacancies during the film growth (more details in Section 2.4). To directly relate its Mn valence to the cation stoichiometry, the oxygen nonstoichiometry in the second sample

was firstly removed by high temperature oxygen annealing. Note that after this initial annealing step, further annealing had no effect on the transport and magnetic properties of the manganite film, indicating that the oxygen content has quickly reached saturation in a chemical equilibrium state. The TEM specimen of the reference and annealed samples had relatively uniform cross-sectional thickness of about 40 nm in the studied area, as calculated with low-loss EELS. Here, we analyze the core loss EELS of the different elements.

The Mn $L_{2,3}$ edge represents the electron transition from Mn $2p_{1/2}$ and $2p_{3/2}$ to unfilled 3d states. A well-established technique to study the Mn valence is the use of the L_3/L_2 peak ratio in the EELS spectrum. This ratio has been shown to decrease monotonically when the oxidation state changes from +2 to +7.[23,24] Chemical shifts also occur upon varying the Mn oxidation state, however, given the experimental difficulty of accurately calibrating the energy scale, we will not use the Mn $L_{2,3}$ peak shift to study the oxidation state. **Figure 2** displays the Mn $L_{2,3}$ edges of the annealed and the reference samples after power-law background subtraction, recorded along film growth direction. By normalizing the L_2 peaks in Figure 2b,d, a direct visual comparison can be made of the L_3/L_2 ratio at different locations. It is clear that the L_3 peak intensity remains constant from the interface to the middle of the annealed film and then gradually increases towards the surface. However, the variation of the Mn L_3 peak intensity in the reference sample is negligible, as indicated by the two parallel red lines in Figure 2d. To quantitatively analyze the Mn valence, the Hartree-Slater cross section function (which is available in Gatan's Digital Micrograph software) is used as a step function to remove the continuum contribution. A 10 eV wide energy window after the L_2 edge is used for scaling purposes. Then, the remaining signals under the L_2 and L_3 lines are integrated within two 11 eV wide windows. Finally, the resulting integrated intensity values are used to calculate the $L_{2,3}$ (L_3/L_2) area ratio for a quantitative analysis of the Mn valence. The reference data we use is from Varela et al. who use the same analysis method.[24] Our calculated $L_{2,3}$ values and the corresponding Mn valence of the annealed and reference samples are plotted in **Figure 3**a,b as a function of distance from interface. The Mn valence in the annealed sample remains about 3.6 from the film-substrate interface to the middle of the film and then decreases to 3.2 closer to the surface, while the reference sample has a uniform Mn valence of 3.2 from interface to surface. To calibrate the EELS Mn nominal valence V_{Mn} at the surface, we use XPS, measuring the Mn 3s splitting energy ΔE_{3s} of the top 5 nm surface of the annealed LSMO film using the equation[25,26]

$$V_{Mn} = 9.67 - \frac{1.27\Delta E_{3s}}{eV}.$$

The XPS result in Figure 3c shows that ΔE_{3s} is 5.1 eV, giving a V_{Mn} of 3.2, which is consistent with the EELS results.

Another method to study the Mn oxidation states is by analyzing the fine structure of the EELS oxygen K-edge. In the dipole approximation, the oxygen K-edge fine structure contains information on excitations from O 1s electrons to 2p bands. Three main features are found in the EELS fine structure: a pre-peak at about 530 eV, the first main peak around 535 eV which arises from the oxygen hybridization with La 5d and Sr 3d bands, and the second main peak at about 540 eV, where the Mn 4sp bands contribute.[27] The pre-peak has a strong contribution from the Mn 3d bands and is sensitive to Mn 3d e_g state occupancies, since the Mn 3d t_{2g} state is fully occupied. Hence, information about Mn 3d band occupancy (i.e., Mn valence) will be exacted by pre-peak analysis. As was demonstrated by Varela et al., the energy separation between pre-peak and adjacent main peak, ΔE, linearly increases with the Mn valence.[24] This effect is attributed to the difference in chemical potential between the initial core and final states of the ejected electrons.[28] The oxygen K edge EELS images in **Figure 4**a show that ΔE stays constant from the interface to the middle part of the annealed film and then decreases linearly until the surface, showing the same trend for the Mn valence as we observed earlier with the Mn $L_{2,3}$-edge. ΔE in the reference sample does not change significantly. The exacted ΔE values are shown in Figure 4b, the whole reference sample and the surface region of the annealed sample have similar ΔE values located around 5.3 eV. Thus we can tell that these two parts have almost the same Mn valence. Since oxygen ions bond with La, Sr and Mn, the overall

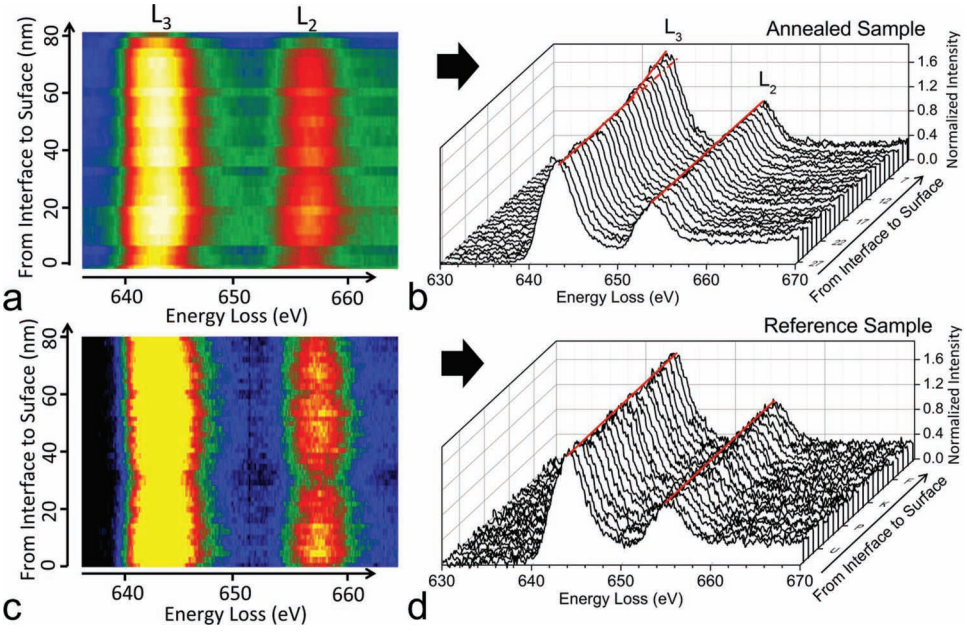

Figure 2. EELS spectrum line scans of the Mn $L_{2,3}$ edges. a,c) Raw EELS profiles of the Mn $L_{2,3}$ edges in the annealed sample and the reference sample, respectively. b,d) The same line scans of the Mn $L_{2,3}$ edge, now with the L_2 peak intensity normalized. The red line shows the variation of the L_3/L_2 peak intensity ratio.

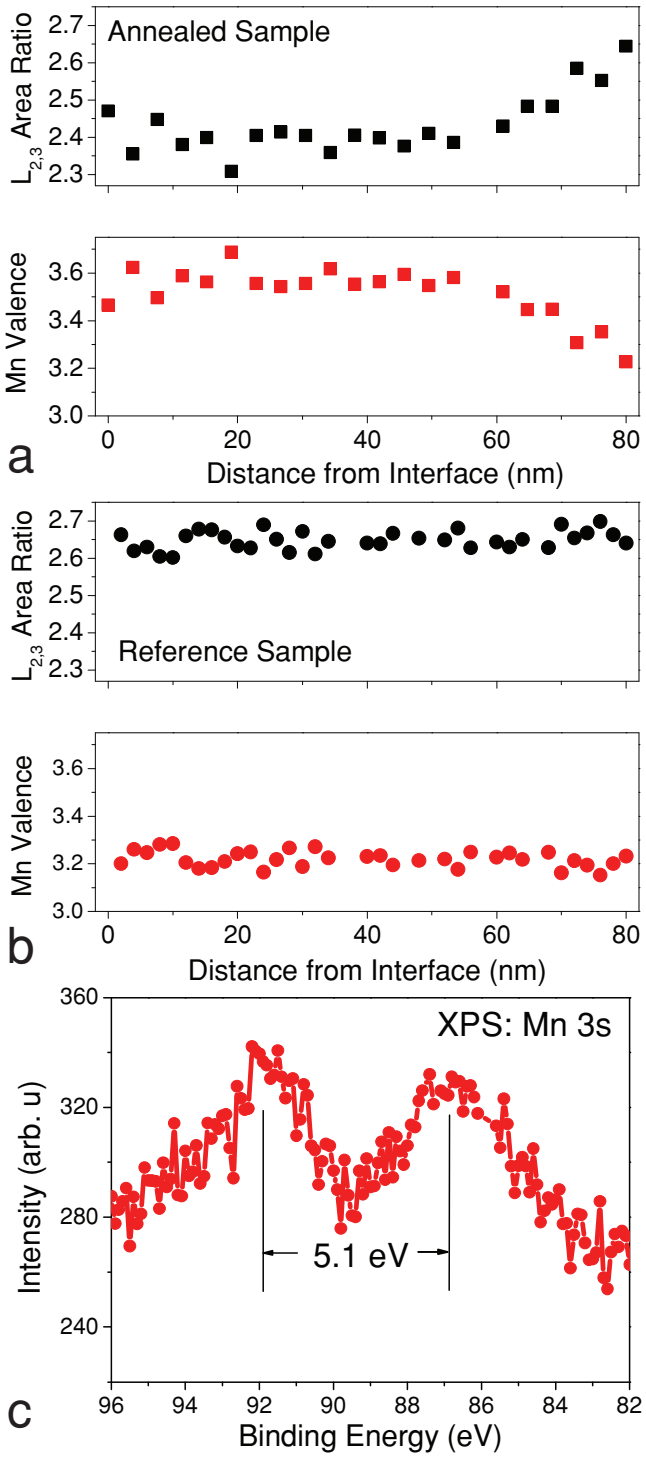

Figure 3. Variation of the Mn nominal valence in LSMO films. a,b) The extracted $L_{2,3}$ ratio (black) and corresponding Mn valence (red) vs. the distance from the interface for a) the annealed sample and b) the reference sample. c) The XPS peak of the Mn 3s band in the annealed sample. The energy separation between two peaks indicates ΔE_{3s}.

oxygen bonding is quite complicated in LSMO, so the change of oxygen K-edge fine structure is presented here merely to verify the concurrent Mn valence change.

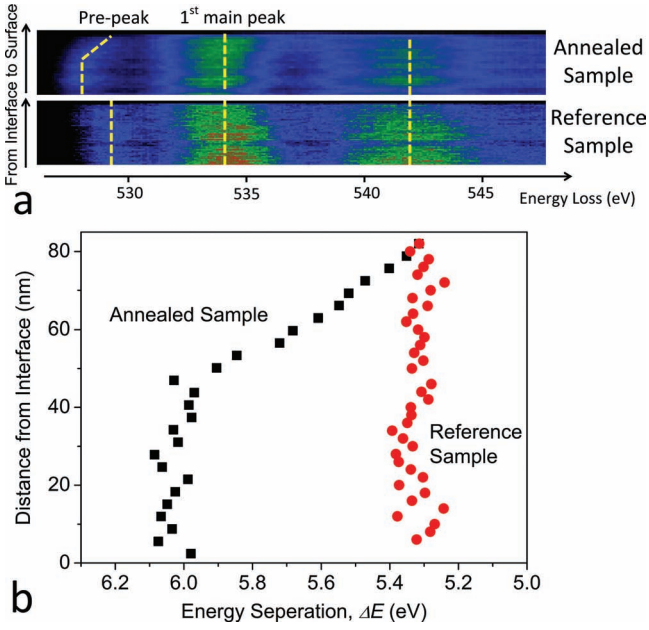

Figure 4. Variations in the oxygen bonding in the annealed and reference samples. a) EELS spectrum line scans of the oxygen K-edge, the dotted lines indicate the intensity maxima. b) The extracted energy separation between the pre-peak and the first main peak.

Mn ions with high oxidation states are supposed to be quite sensitive to electron beam degradation. Riedl *et al.* studied the $La_{0.7}Sr_{0.3}MnO_3$ films in which they acquired EELS with increasing electron dose.[29] They found that, with the dose beyond the threshold for damage, the EELS O K pre-peak nearly disappears and the intensity of the third peak is only 10% greater than the minimum following the second peak. Correspondingly, the ratio of the maximum intensity of Mn L_2 peak to L_3 peak falls from 0.6 to 0.4. Compared with the results of Riedl et al., the oxygen pre-peaks in our spectra presented in Figure 4a,c are strong and the intensity of the third peak is around 60% greater than the minimum following second peak for the whole LSMO layer. Accordingly, the ratio of maximum of Mn L_2 to L_3 peaks is around 0.6. As such, we observed no evidence for electron beam induced damage. Additionally, the high-angle annular dark-field (HAADF) scanning TEM (STEM) image taken after the EELS line scans showed no sample damage. Therefore, we rule out electron beam damage as cause for the observed EELS fine structure modulations in our experiment.

To investigate the local cation stoichiometry, we analyze the EELS signal of the La $M_{4,5}$, Sr $M_{4,5}$, Mn $L_{2,3}$, and O K-edges and use the normalized EELS intensity to exact the elemental profiles across the LSMO films, shown in **Figure 5**. By normalizing the intensities, we obtain relative profiles for each element. As the sample is fully oxygen annealed at high temperature for 5 hours, the oxygen nonstoichiometry is removed; further details are shown in the Supporting Information (see Supporting Information). Figure 5a shows that the annealed sample has excess La near the film-substrate interface, after which its content reduces towards the surface. From the relative content of La and Sr in Figure 5b, there can be no segregation between

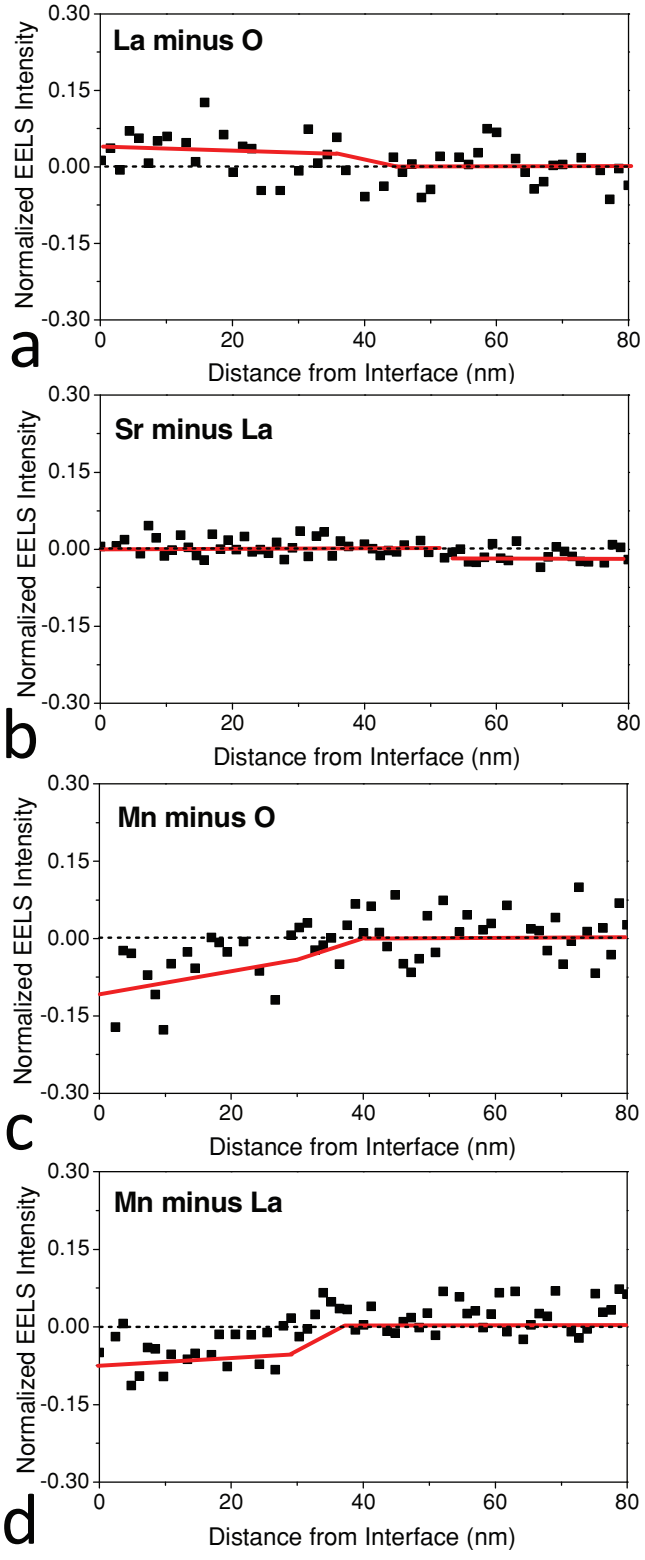

Figure 5. Relative distribution of the chemical elements in the annealed LSMO films. Intensity difference from normalized EELS line scans a) between the elements La and O, b) between Sr and La, c) between Mn and O, and d) between Mn and La.

A-site cations near the interface, but the Sr content decreases somewhat near the surface. Combined with the experimental results in the next section, this observation can be explained by the migration of Sr cations towards the surface during growth, with the tendency of forming a SrO monolayer. Figure 5c,d show that Mn is deficient compared with La and O near the interface, and then increases towards the surface in the annealed sample. However, as demonstrated in the Supporting Information, the cation gradient mentioned above is absent in the reference sample, as its relative profiles of each element are all around zero (see Supporting Information).

In analytical TEM, one needs to be careful with the quantitative interpretation of the EELS signal. As was shown earlier, the limited collection angle of EELS can lead to quantification artifacts when the thickness or density of the specimen locally varies.[30] To give a complete chemical picture of our specimen, energy-dispersive X-ray spectroscopy (EDX), a technique that is much less sensitive to such artifacts, is employed to provide additional information on the elemental distribution. Details about the EDX results are given in the Supporting Information. The uniform distribution of oxygen throughout the two samples, and the manganese deficiency near the film/substrate interface in the annealed sample are demonstrated. The results confirm our EELS results, supporting the validity of the conclusions that were drawn from Figure 5a–d. It can therefore be concluded that near the interface, the A-site cations (La and Sr) are in excess, while the Mn cations are deficient in the annealed sample. Thus, proportional A-site cations have moved to the B-sites during growth to substitute Mn cations.[16,31] As the film becomes thicker, the A-site/B-site cation ratio recovers to the nearly nominal value. As the oxygen content is uniform throughout the film, the cation stoichiometry is suggested to dominate the observed gradient of Mn valence. With excess of A-site cations and deficiency of Mn cation near the manganite/substrate interface, the Mn valence should be higher to maintain the charge neutrality, which was confirmed in Figure 3. As a comparison, the mentioned cation nonstoichiometry disappears in the reference sample grown under high oxygen pressure, thus we can conclude that the oxygen vacancies during growth play a dominant role in modifying the cation stoichiometry. The discussion section will propose a mechanism that can explain the local chemical variations.

2.3. The Strontium Surface Segregation

The second type of cation nonstoichiometry that occurs during growth is the off-stoichiometric ratio between La and Sr near the film surface. This modification of the surface chemical composition might severely affect the interface properties of manganite-based tunnel junction devices. As observed by other research groups, Sr surface segregation is the most likely surface cation nonstoichiometry.[18,32] Utilizing the surface-sensitive angle-dependent X-ray photoelectron spectroscopy (XPS) and element-sensitive Z-contrast STEM imaging with atomic resolution, we here investigate the relationship between Sr surface segregation and oxygen vacancies. **Figure 6**a,b show the XPS Sr 3d peaks of the annealed with normal and grazing

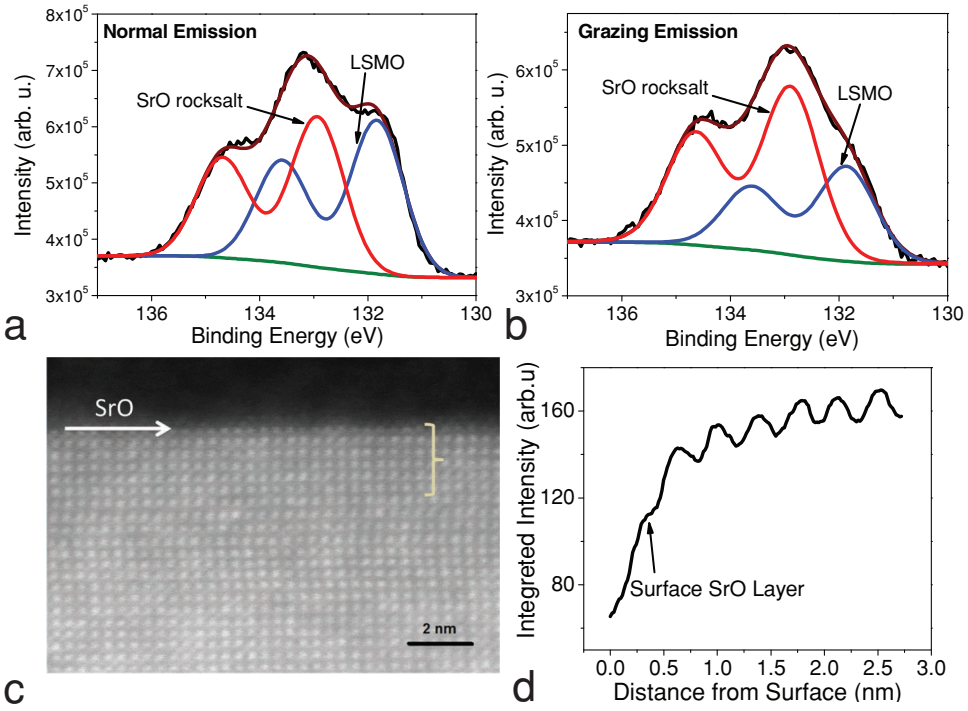

Figure 6. Surface analysis of the annealed LSMO film. a) Angle-dependent XPS of the annealed sample, collected with normal emission of photoelectrons, showing the Sr 3d band. b) Angle-dependent XPS, collected with grazing emission of photoelectrons. As grazing emission of photoelectrons are more sensitive to the surface content, we can see the surface of LSMO is covered with SrO in rock-salt phase. c) HAADF-STEM image (Z-contrast image) from the surface region of LSMO. d) Integrated intensity profile of the HAADF-STEM image near the surface, integrated from a 10 nm wide area of the top 3 nm.

emission of photoelectrons respectively, the latter being more sensitive to surface composition due to the finite escape depth of photoelectrons. After the deconvolution of Sr 3d peaks, two peak doublets are found in the spectrum of the annealed sample. Based on the literature,[32] we assign the peaks with higher binding energy (around 135 eV) to Sr 3d in SrO rock-salt phase, and the lower binding energy (133.5 eV) to Sr 3d in perovskite. The XPS results show that the annealed sample has both surface segregated SrO phase and perovskite underneath. The increased signal for the SrO rock-salt structure in the grazing emission spectrum suggests that SrO is located at the topmost 1 nm, as the X-ray detection depth here is less than 1 nm for the used photon energy of 220.8 eV. The Z-contrast STEM image in Figure 6c shows that the topmost monolayer, indicated by the arrow, has lower intensity in comparison with the more uniform intensity of the layers below. The integrated Z-contrast intensity profile in Figure 6d shows this effect in more detail. As the contrast in the HAADF-STEM image is proportional to approximately $Z^{1.7}$ (with Z as the atomic number) and La has larger atomic number than Sr, it can be concluded that the outermost atomic layer has more Sr cations. Combined with the EELS chemical profile from Figure 5b, it is concluded that the Sr atoms diffuse to the top surface to neutralize the surface charge,[33] resulting in slightly decreased Sr content in the perovskite underneath, and a monolayer of SrO at the surface.

However, the thermal annealing effect might also induce Sr diffusion towards the surface, and needs to be considered as well. To verify this, the surface of the as grown LSMO film deposited under low oxygen pressure was also characterized by angle-dependent XPS. **Figure 7**a,b show the XPS Sr 3d band of the as-grown LSMO film with induced oxygen vacancies. Similar to the annealed sample, two peak doublets are observed, demonstrating that the SrO rock-salt phase is not developed by post-deposition annealing. Figure 7c,d present the XPS Sr 3d band of the reference sample. There is only one doublet, assigned to the pure perovskite phase.[32] As mentioned earlier, the cation mobility is strongly limited by the high activation barrier in the close-packed perovskite structure,[12] thus, although the XPS experiments were not done in-situ in the film growth chamber, just the exposure of the sample to the atmosphere cannot supply enough thermal energy to jump the activation barrier for cation diffusion, to modify the surface cation stoichiometry. From the clear difference in the XPS of all three samples, it is therefore concluded that the oxygen vacancies during growth determine the observed Sr surface segregation.

2.4. Magnetic and Transport Properties

In order to understand the interplay of the observed cation stoichiometry and the properties of LSMO films, transport and magnetic measurements were performed. The electrical and ferromagnetic properties of LSMO are dominated by the double-exchange mechanism,[34] where the Mn e_g electrons hop between Mn^{3+} and Mn^{4+} cations when their spins are parallel. Therefore, the Mn nominal valence which represents the Mn^{3+}/

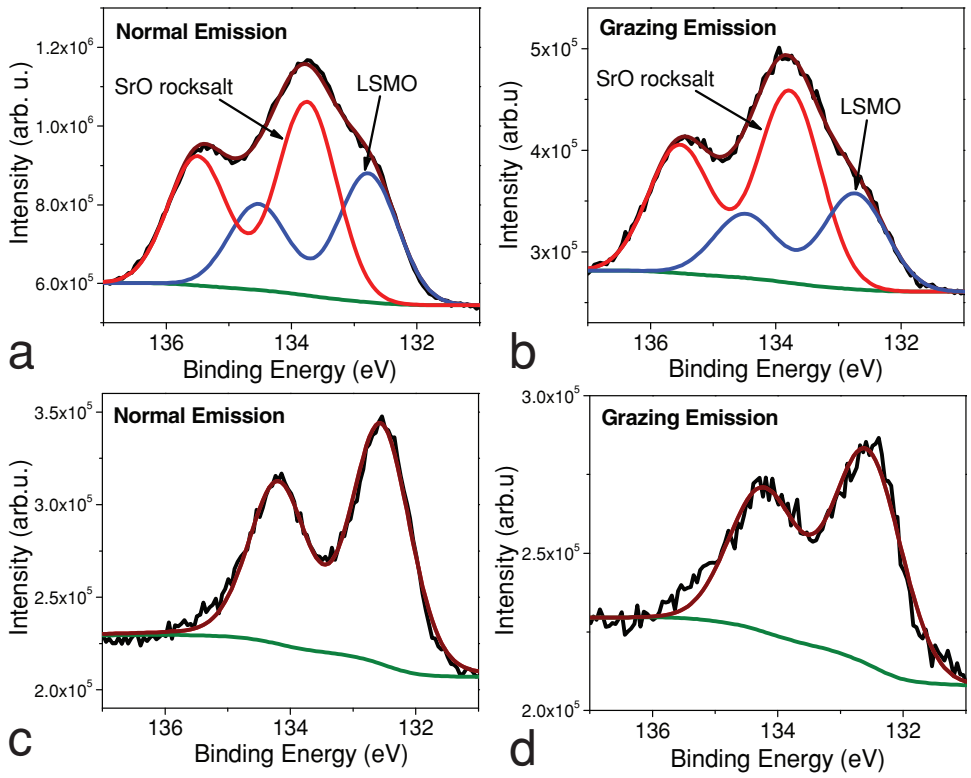

Figure 7. Surfaces of LSMO film grown under low oxygen pressure before annealing and the reference sample, grown under high oxygen partial pressure. a) Angle-dependent XPS of the Sr 3d bands, with normal emission and b) with grazing emission of photoelectrons from the as grown sample under low oxygen pressure. c) With normal emission, and d) grazing emission of photoelectrons from the reference sample grown under high oxygen pressure.

Mn^{4+} ratio, plays a crucial role in determining these properties. **Figure 8**a shows the magnetic hysteresis loops of an annealed sample and of a reference sample, measured at 5 K. The coercivity of the annealed sample is 526 Oe, while that of the reference sample is only 98 Oe. The saturation magnetization of the annealed sample is 50% lower than that of reference sample which exhibits bulk values around 550 emu cm^{-3}.[22] This shows that the Mn valence and composition of the manganite films grown under high oxygen pressure give nearly nominal values, while the annealed sample maybe severely off chemical stoichiometry. Interestingly, pronounced multistep magnetization reversal processes are observed in the magnetic hysteresis loop of the annealed sample, while the reference sample displays a square-like loop. This difference may result from the inhomogeneity of the magnetic phases in the annealed sample. According to the magnetic phase diagram, LSMO is expected to be nonferromagnetic when the Mn valence is at least + 3.6 (60% Mn^{4+}, 40% Mn^{3+}), and ferromagnetic when the Mn valence is below + 3.5.[35] Therefore, it is reasonable to assume that the annealed LSMO layer near the interface is nonferromagnetic while it becomes ferromagnetic closer to the free surface. This assumption is supported by Infante et al.,[36] who observed the nonferromagnetic phase at the La-enriched interface and Sr-enriched surface of (La,Ca)MnO_3 films. The existence of a nonferromagnetic phase explains the suppression of magnetization in the annealed sample, while the enhanced coercivity could then be attributed to the pinning of magnetic domains by the nonferromagnetic phase near the interface. Figures 8b-d show that the Curie temperature (*Tc*) of the annealed sample is around 130 K and the magnetoresistance is 400% at 7 Tesla, while respective values of 290 K and 180% are found for the reference sample. Additionally, there is a magnetic transition around 25 K in the magnetization vs. temperature (*M-T*) curve of the annealed sample, suggesting the existence of a supplementary magnetic phase at low temperature. The differences in the resistivity vs. temperature (*R-T*) curves between the as-grown (with oxygen pressure of 1 Pa) and the post-annealed samples are quite dramatic, due to the existence of oxygen vacancies during film growth. Further oxygen annealing has no effect on the magnetic and electrical properties, which shows that the oxygen content achieves a chemical equilibrium state. This observation confirms the EDX results in Supporting Information. As the Curie temperature of the annealed sample remains suppressed, nonstoichiometry of the cations in the film is suggested.

2.5. Discussion

We will now discuss the underlying mechanism for the tunable cation nonstoichiometry by oxygen vacancies. As mentioned by Muller et al. and Kourkoutis et al.,[13,14] A-site cation excess can be induced by high laser fluence during PLD growth. However,

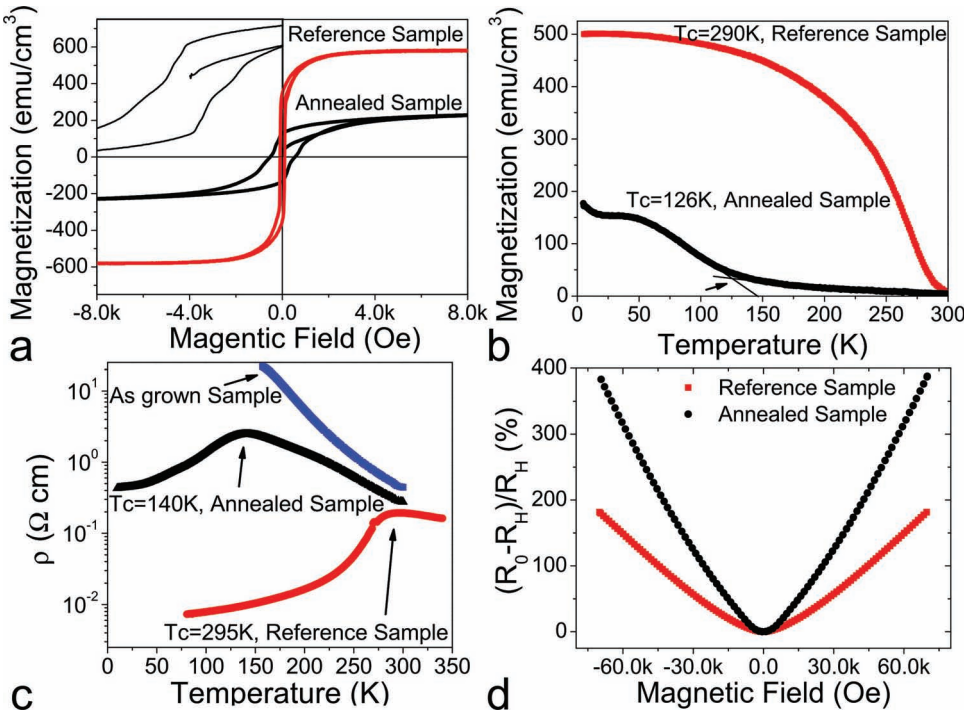

Figure 8. Magnetic properties of LSMO. a) Magnetic hysteresis loop at 5 K. The inserted graph is a magnification of the magnetic hysteresis loop from the annealed sample, showing the multistep magnetization reversal processes. b) *M-T* curves. c) *R-T* curve. d) Magnetoresistance plot with applied magnetic field along the (001) plane.

they did not observe significant changes in the Mn or Ti valence states in very thin stacks of epitaxial layers. Estradé et al. on the other hand, demonstrated that the Ca/La ratio and Mn valence gradually decreased from $La_{0.7}Ca_{0.3}MnO_3$/STO interface to the free surface, which was solely dominated by stress accommodation.[37] In our experiments on epitaxial LSMO films, the variation of Mn valence with opposite trend across the film is evidently demonstrated, in support of the model that the oxygen vacancies during film growth are indeed another important source of local cation nonstoichiometry.

The existence of oxygen vacancies during growth will locally generate extra positive charges. Together with the strain tensor towards the oxygen vacancy, the oxygen octahedron can be elongated and rotated.[38] As a result, the available space increases for B-site cations nearest to the oxygen vacancies, which will allow accommodation of larger cations such as La and Sr in B-sites.

At the initial growth period, the substitution of Mn cations (with oxidation states of +3 or +4) by La and Sr cations (with oxidation states of +3 and +2, respectively) in B-sites can generate negative charge to neutralize the positive charge induced by oxygen vacancies. Meanwhile, the accommodation of large La and Sr cations in B-sites can increase the lattice constant and relieve some of the tensile strain induced by the $SrTiO_3$ substrate. As the growing film gets thicker, the epitaxial tensile strain is abated and becomes insufficient to accommodate the large A-site cations in the B-sites. Thus, the proportion of Mn substitution by La/Sr cations reduces. The Sr migration towards the film surface becomes the dominate mechanism of cation nonstoichiometry instead. The positive charge induced by oxygen vacancies near the growing surface may favor Sr segregation for electroneutrality.[33] Based on the fact that there is a depletion of Mn content near the interface region, the refilling of oxygen vacancies after annealing can in fact increase the amount of negative charge and then result in larger variation of the Mn valence (to maintain local charge neutrality). As one intriguing consequence, high Mn nominal valence (+3.6) exists in the strained film near the substrate, and remains constant within a thickness of about 45 nm, beyond which it decays monotonically to 3.2 until the free surface. Therefore it is concluded that the oxygen vacancies can induce the cation nonstoichiometry, resulting in a nonmagnetic and insulating layer near the interface, which will hinder the device application of such a film.

Furthermore, as the magnetic properties are determined by the Mn nominal valence,[34,39] the observed inhomogeneity of Mn valence in the annealed sample is expected to enhance magnetic phase separation. Earlier published results show that Mn^{4+} is in excess near the interface in $La_{2/3}Ca_{1/3}MnO_3$ films due to interface reconstruction, leading to insulating and nonmagnetic phases within a thickness of less than 5 nm.[40,41] However, our work shows a nonmagnetic region with excess Mn^{4+} (with Mn nominal valence of 3.6) with a thickness around 45 nm, which in this case is 50% of the whole sample volume. The comparison confirms that there is more than one source of the observed excess Mn^{4+} near interface. As an extrinsic mechanism, oxygen vacancies during growth can also induce cation nonstoichiometry, generate interfacial dead layers, and cover

the intrinsic effect from interface reconstruction. Only by carefully selecting the appropriate oxygen pressure and minimizing the oxygen vacancies to the lowest degree, will the interfacial dead layer be reduced.

Finally, the second cation nonstoichiometry that forms the SrO rock-salt surface monolayer might in fact provide a new prospect for the fabrication of high performance tunnel devices. As an insulating material, SrO can serve as an extra tunnel barrier when LSMO is integrated into tunnel junctions. Meanwhile, the cation ratio in the underlying perovskite phase is also off-stoichiometric. These will account for the reduction of the Curie temperature and spin transport properties near the LSMO-barrier interface. Therefore, this observed surface cation off-stoichiometry might explain a previous report demonstrating that the transport and magnetic properties of a LSMO/STO multilayer can be improved by adding a $LaMnO_3$ layer between LSMO and STO.[42] This present work suggests that the $LaMnO_3$ layer in that work played the role of compensating the cation off-stoichiometry that was induced by strontium segregation.

3. Conclusion

In summary, our findings establish two types of cation nonstoichiometry, modified by oxygen vacancies during LSMO film growth. At the initial growth stages near the $SrTiO_3$ substrate, the A-site cations (La/Sr) partially substitute Mn. At a later stage after most lattice strain is relieved, Sr migrates towards the film surface, and produces a SrO rock-salt monolayer. The resulting long-range inhomogeneity of the Mn valence in the annealed $La_{0.8}Sr_{0.2}MnO_3$ films along the film growth direction was demonstrated here with EELS. It was found that high Mn nominal valence (+3.6) exists in the strained film near its substrate, and remains constant within a thickness of about 40–45 nm, beyond which it decays monotonically until the free surface. The suppressed magnetization and increased magnetoresistance in this epitaxial film is attributed to the nonferromagnetic phase near the $SrTiO_3$ - $La_{0.8}Sr_{0.2}MnO_3$ interface due to this cation nonstiochiometry. The magnetic hysteresis loop of the annealed sample presents multistep magnetization reversal processes, indicating enhanced inhomogeneity of the magnetic phase. These results demonstrate the importance of oxygen vacancies during growth as a source of cation nonstoichiometry near the interface and surface of epitaxial thin films. With regard to tunneling devices, the oxygen vacancies in LSMO during growth can generate an extra insulating and nonmagnetic layer near LSMO-barrier interfaces, leading to the reduction of the Curie temperature and conductivity.

4. Experimental Section

An 80 nm thick $La_{0.8}Sr_{0.2}MnO_3$ (LSMO) film was grown epitaxially on $SrTiO_3$ (001) (STO) substrate by pulsed laser deposition (PLD) with an energy density of 1.5 J cm^{-2} and repetition of 1 Hz. The target material was made by the conventional solid state route using stoichiometric amounts of La_2O_3, Mn_2O_3 and $SrCO_3$ as initial reagents. Powder X-ray diffraction analysis showed that the final target was single phase without any impurity peaks. For the annealed sample, the oxygen partial pressure was set to 1 Pa, in order to induce large amount of oxygen vacancies during growth. It was grown at a temperature of 780 °C and then post-annealed in a tube furnace at 900 °C for 5 h under oxygen flux twice. Transport properties measurements as a function of temperature were conducted after each annealing. As there were no differences in the resistivity and metal to insulator transition temperature, the elimination of oxygen nonstoichiometry can be recognized. The details of both in situ reflected high energy electron diffraction (RHEED) and ex situ high resolution X-ray diffraction (HRXRD) analysis of the as-grown sample are described elsewhere.[17] In order to verify the effect of oxygen vacancies, the reference LSMO film with the same composition was grown under the much higher oxygen pressure of 26 Pa, while the other growth parameters were kept the same. TEM specimens were prepared by grinding, dimpling, and ion milling in a Gatan Precision ion polishing system. The specimens were briefly cleaned in oxygen plasma, and transferred directly into the microscope for observation. High resolution transmission electron microscopy (TEM) and selected area electron diffraction (SAED) were performed on a JEOL-2100F microscope, operated with an electron acceleration voltage of 200 kV. An FEI Titan TEM with Schottky emitter, also operated at 200 kV, with an attached EDAX EDX detector and a Gatan Tridiem ER EELS detector was employed for EDX and EELS line scans with probe size of 0.5 nm and 2.6 nm steps, in scanning TEM (STEM) mode.

The surface Mn 3s electron band analysis was carried out by X-ray photoelectron spectroscopy (XPS) using a VG ESCALAB 220i-XL spectrometer with an Al $K\alpha$ monochromatic X-ray source (1486.6 eV). The XPS characterization of Sr 3d was performed at beam line SINS, located in the Singapore Synchrotron Light Source. The incoming X-ray energy was 220.79 eV and the energy resolution 0.2 eV. The Sr 3d spectra with both normal incidence and grazing X-ray incidence were compared to measure the surface Sr content. A Quantum Design physical properties measurement system (PPMS) was used to characterize the magnetic and transport properties. The *M-H* curve was measured at 5 K with the magnetic field applied in-plane, while the magnetoresistance was measured at their metal-to-insulator transition temperatures, 140 K and 290 K for annealed and reference samples, respectively.

Supporting Information

Supporting Information is available from the Wiley Online Library or from the author.

Acknowledgements

Fruitful technical discussions with Maria Varela, Lena Fitting Kourkoutis, Bin Xia and Baomin Wang are gratefully acknowledged. This investigation was financially supported by Singapore A*STAR SERC Grant No: 102 101 0019.

Received: January 16, 2012
Revised: March 20, 2012
Published online: June 15, 2012

[1] J. M. D. Coey, M. Viret, S. Von Molnár, *Adv. Phys.* **2009**, *58*, 571.
[2] V. Garcia, M. Bibes, L. Bocher, S. Valencia, F. Kronast, A. Crassous, X. Moya, S. Enouz-Vedrenne, A. Gloter, D. Imhoff, C. Deranlot, N. D. Mathur, S. Fusil, K. Bouzehouane, A. Barthelemy, *Science* **2010**, *327*, 1106.
[3] J. D. Burton, E. Y. Tsymbal, *Phys. Rev. Lett.* **2011**, *106*, 157203.
[4] V. A. Dediu, L. E. Hueso, I. Bergenti, C. Taliani, *Nat. Mater.* **2009**, *8*, 707.
[5] M. Mamak, G. S. Métraux, S. Petrov, N. Coombs, G. A. Ozin, M. A. Green, *J. Am. Chem. Soc.* **2003**, *125*, 5161.

[6] M. Izumi, Y. Ogimoto, Y. Okimoto, T. Manako, P. Ahmet, K. Nakajima, T. Chikyow, M. Kawasaki, Y. Tokura, *Phys. Rev. B* **2001**, *64*, 064429.
[7] K. Dorr, T. Walter, M. Sahana, K. H. Muller, K. Nenkov, K. Brand, L. Schultz, *J. Appl. Phys.* **2001**, *89*, 6973.
[8] F. Yang, N. Kemik, M. D. Biegalski, H. M. Christen, E. Arenholz, Y. Takamura, *Appl. Phys. Lett.* **2010**, *97*, 092503.
[9] J. Son, P. Moetakef, B. Jalan, O. Bierwagen, N. J. Wright, R. Engel-Herbert, S. Stemmer, *Nat. Mater.* **2010**, *9*, 482.
[10] D. J. Keeble, S. Wicklein, R. Dittmann, L. Ravelli, R. A. Mackie, W. Egger, *Phys. Rev. Lett.* **2010**, *105*, 226102.
[11] T. Ohnishi, K. Shibuya, T. Yamamoto, M. Lippmaa, *J. Appl. Phys.* **2008**, *103*, 103703.
[12] M. G. Blamire, J. L. MacManus-Driscoll, N. D. Mathur, Z. H. Barber, *Adv. Mater.* **2009**, *21*, 3827.
[13] D. A. Muller, L. F. Kourkoutis, M. Murfitt, J. H. Song, H. Y. Hwang, J. Silcox, N. Dellby, O. L. Krivanek, *Science* **2008**, *319*, 1073.
[14] L. F. Kourkoutis, J. H. Song, H. Y. Hwang, D. A. Muller, *Proc. Natl. Acad. Sci. USA* **2010**, *107*, 11682.
[15] M. Bosman, V. J. Keast, J. L. García-Muñoz, A. J. D'Alfonso, S. D. Findlay, L. J. Allen, *Phys. Rev. Lett.* **2007**, *99*, 086102.
[16] A. I. Lobad, R. D. Averitt, C. H. Kwon, A. J. Taylor, *Appl. Phys. Lett.* **2000**, *77*, 4025.
[17] T. Kanki, H. Tanaka, T. Kawai, *Phys. Rev. B* **2001**, *64*, 224418.
[18] T. T. Fister, D. D. Fong, J. A. Eastman, P. M. Baldo, M. J. Highland, P. H. Fuoss, K. R. Balasubramaniam, J. C. Meador, P. A. Salvador, *Appl. Phys. Lett.* **2008**, *93*, 151904.
[19] Z. Yang, L. Sun, C. Ke, X. Chen, W. Zhu, O. Tan, *J. Cryst. Growth.* **2009**, *311*, 3289.
[20] O. I. Lebedev, G. Van Tendeloo, S. Amelinckx, B. Leibold, H. U. Habermeier, *Phys. Rev. B* **1998**, *58*, 8065.
[21] M. Zhang, X. L. Ma, D. X. Li, H. B. Lü, Z. H. Chen, G. Z. Yang, *Phys. Status Solidi A* **2003**, *196*, 365.
[22] A. Urushibara, Y. Moritomo, T. Arima, A. Asamitsu, G. Kido, Y. Tokura, *Phys. Rev. B* **1995**, *51*, 14103.
[23] D. B. Loomer, T A. Al, L. Weaver, S. Cogswell, *Am. Mineral.* **2007**, *92*, 72.
[24] M. Varela, M. P. Oxley, W. Luo, J. Tao, M. Watanabe, A. R. Lupini, S. T. Pantelides, S. J. Pennycook, *Phys. Rev. B* **2009**, *79*, 085117.
[25] E. Beyreuther, S. Grafstrom, L. M. Eng, C. Thiele, K. Dorr, *Phys. Rev. B* **2006**, *73*, 155425.
[26] V. R. Galakhov, M. Demeter, S. Bartkowski, M. Neumann, N. A. Ovechkina, E. Z. Kurmaev, N. I. Lobachevskaya, Ya. M. Mukovskii, J. Mitchell, D. L. Ederer, *Phys. Rev. B* **2002**, *65*, 113102.
[27] H. Kurata, C. Colliex, *Phys. Rev. B* **1993**, *48*, 2102.
[28] T. Riedl, T. Gemming, W. Gruner, J. Acker, K. Wetzig, *Micron* **2007**, *38*, 224.
[29] T. Riedl, T. Gemming, K. Wetzig, *International Workshop on Enhanced Data Generated by Electrons (EDGE 2005)*, Grundlsee, Austria **2005**.
[30] M. Bosman, Y. Zhang, C. K. Cheng, X. Li, X. Wu, K. L. Pey, C. T. Lin, Y. W. Chen, S. H. Hsu, C. H. Hsu, *Appl. Phys. Lett.* **2010**, *97*, 103504.
[31] J. Mizusaki, N. Mori, H. Takai, Y. Yonemura, H. Minamiue, H. Tagawa, M. Dokiya, H. Inaba, K. Naraya, T. Sasamoto, T. Hashimoto, *Solid State Ionics* **2000**, *129*, 163.
[32] R. Bertacco, J. P. Contour, A. Barthélemy, J. Olivier, *Surf. Sci.* **2002**, *511*, 366.
[33] W. A. Harrison, *Phys. Rev. B* **2011**, *83*, 155437.
[34] C. Zener, *Phys. Rev.* **1951**, *82*, 403.
[35] Y. Tokura, Y. Tomioka, H. Kuwahara, A. Asamitsu, Y. Moritomo, M. Kasai, *J. Appl. Phys.* **1996**, *79*, 5288.
[36] I. C. Infante, F. Sanchez, J. Fontcuberta, M. Wojcik, E. Jedryka, S. Estradté, S. Peiro, F. J. Arbiol, V. Laukhin, J. P. Espinos, *Phys. Rev. B* **2007**, *76*, 224415.
[37] S. Estradé, J. Arbiol, F. Peiró, I. C. Infante, F. Sánchez, J. Fontcuberta, F. de la Peña, M. Walls, C. Colliex, *Appl. Phys. Lett.* **2008**, *93*, 112505.
[38] D. A. Freedman, D. Roundy, T. A. Arias, *Phys. Rev. B* **2009**, *80*, 064108.
[39] Z. Fang, I. V. Solovyev, K. Terakura, *Phys. Rev. Lett.* **2000**, *84*, 3169.
[40] M. Bibes, L. Balcells, S. Valencia, J. Fontcuberta, M. Wojcik, E. Jedryka, S. Nadolski, *Phys. Rev. Lett.* **2001**, *87*, 067210.
[41] A. Tebano, C. Aruta, S. Sanna, P. G. Medaglia, G. Balestrino, A. A. Sidorenko, R. De Renzi, G. Ghiringhelli, L. Braicovich, V. Bisogni, N. B. Brookes, *Phys. Rev. Lett.* **2008**, *100*, 137401.
[42] H. Yamada, Y. Ogawa, Y. Ishii, H. Sato, M. Kawasaki, H. Akoh, Y. Tokura, *Science* **2004**, *305*, 646.